Creep rupture of fiber bundles: A molecular dynamics investigation

G. Linga,[1] P. Ballone,[1,2] and Alex Hansen[1]
[1]*Department of Physics, Norwegian University of Science and Technology, N-7491 Trondheim, Norway*
[2]*Center for Life Nano Science @Sapienza, Istituto Italiano di Tecnologia, Rome, Italy*
(Received 7 April 2015; published 10 August 2015)

The creep deformation and eventual breaking of polymeric samples under a constant tensile load F is investigated by molecular dynamics based on a particle representation of the fiber bundle model. The results of the virtual testing of fibrous samples consisting of 40 000 particles arranged on $N_c = 400$ chains reproduce characteristic stages seen in the experimental investigations of creep in polymeric materials. A logarithmic plot of the bundle lifetime τ versus load F displays a marked curvature, ruling out a simple power-law dependence of τ on F. A power law $\tau \sim F^{-4}$, however, is recovered at high load. We discuss the role of reversible bond breaking and formation on the eventual fate of the sample and simulate a different type of creep testing, imposing a constant stress rate on the sample up to its breaking point. Our simulations, relying on a coarse-grained representation of the polymer structure, introduce new features into the standard fiber bundle model, such as real-time dynamics, inertia, and entropy, and open the way to more detailed models, aiming at material science aspects of polymeric fibers, investigated within a sound statistical mechanics framework.

DOI: 10.1103/PhysRevE.92.022405 PACS number(s): 62.20.Hg, 81.05.Lg, 46.50.+a, 83.60.La

I. INTRODUCTION

The irreversible deformation and eventual breaking of materials are paradigmatic phenomena of great practical and conceptual importance, since they are part of our everyday experience, play a fundamental role in engineering, and display a range of properties from cooperativity to extreme nonlinearity that still challenge our ability to model and understand them. The applied interest and widespread occurrence have undoubtedly driven early investigations [1,2] of these phenomena right up to the present day status as a mature field [3–7]. Over the past couple of decades, the interest in such phenomena has been revived by the advent of the computer as a serious research tool [8–10].

The physics community view of fracture has been greatly influenced by its analogies with phase transitions and critical phenomena [10]. Thus, universality and scaling relations provided the first and foremost framework to interpret experimental results [11–14]. From the theoretical point of view, these approaches have the additional appeal of providing useful and concise information without referring to the details of the molecular structure and interatomic interactions.

Over the past few years, atomistic modeling has matured to the point where materials may be modelled computationally from the atomic scale up to the level where continuum theories get a foothold [15], strengthening the tie between theory or computer modeling using simple models and experiments.

Technological advances, however, aim at optimizing the choice and possibly improving the performance of materials. By necessity, these efforts target system-specific properties and thus non-universal aspects of mechanical response to perturbations. Moreover, the recent advent of atomistic modeling provides increasing opportunities for a chemical-physics analysis of fracture. Models going beyond scaling relations and universality considerations are required also to investigate finite and sometimes small systems, whose dimensions might approach the nanometric scale [16].

We focus here on the fracture of polymeric fibers under a steady tensile load, partly because of applied interest that is enhanced by the role of creep. Even more, we are motivated by the intrinsic interest of highly anisotropic and viscoelastic materials, whose response to an applied stress depends on entropy as much as on enthalpy.

The theoretical analysis of the failing of fibrous systems relies heavily on the so-called fiber bundle model [17–20] which has proven itself both as a simple but paradigmatic model for failure in much the same way the Ising model is for magnetism, and as a model for detailed calculation of the strength of fiber-reinforced composites [21,22]. Interpreting the failure of polymers in the context of the fiber bundle model one combines probability distributions p_1 of elementary processes such as the breaking of an individual intermolecular link to predict the time evolution of large (ideally infinite) assemblies of chains. The many-particle behavior is introduced by defining the redistribution of load upon breaking of chains, while temperature and material properties only enter the definition of the probability distribution of the elementary processes. The final aim is, e.g., the prediction of the bundle lifetime $\langle\tau\rangle$ and of fluctuations of breaking times around $\langle\tau\rangle$ [20,23].

Going deeper than these models are capable of requires investigations at the atomistic level, for which sophisticated methods are available, up to *ab initio* simulation [24]. However, the multiscale character of these processes makes them very difficult to model. Moreover, most of these detailed models and methods are tuned on near-equilibrium conditions, and their accuracy and reliability is virtually untested for the large deformations relevant in this context.

We report here results from the computational exploration of a particle-based realization of finite chains made of discrete particles grafted to two parallel rigid clamps. Hence, the system is related to the equal-load-sharing fiber bundle [17,18]. The results are compared to standard theoretical approaches and to fracture experiments on protein gels [25].

In our approach, the rate of bond and of chain breaking is not an empirical input as in the standard fiber bundle model, but it is implicitly determined by the parameters entering the definition of the interparticle potential, and by the thermodynamic conditions. Moreover, the results of our

 ©2015 American Physical Society

simulations based on real-time dynamics, reveal intriguing cooperative effects and correlations among breaking events. In this respect, our study differs in an essential way from previous studies devoted to the simulation of single chains [26–28].

In the next section, we describe in detail our model and its numerical implementation. In Sec. III, we present our results. Our main result is that the average lifetime τ of the bundles scale as F^{-4} at high F, where F is the load on the rigid plates to which the chains are anchored. Section IV contains a summary of our results and the conclusions we draw from them.

II. MODEL AND METHOD

The system under study consists of N_c polymeric chains attached to two parallel planar surfaces perpendicular to the z axis, located at z_a and z_b. For the sake of definiteness, we assume that our system is oriented in such a way that $z_b \geqslant z_a$, with $L_z = z_b - z_a$ measuring the instantaneous length of the bundle.

Each chain is made of N_b regular beads, and two special beads, representing the opposite end points. These two special beads are constrained to lay on the boundary planes but otherwise are free to move along x and y. The link between each end point and the nearest regular bead is harmonic:

$$V_w(|\mathbf{r_w} - \mathbf{r_1}|) = \tfrac{1}{2} K_w |\mathbf{r_w} - \mathbf{r_1}|^2 \tag{1}$$

and, as such, it cannot be broken. In the equation above, $\mathbf{r_w}$ and $\mathbf{r_1}$ are the coordinates of the end point and its first neighbor, respectively.

Regular beads interact only with their nearest neighbors along the chain through a truncated Morse potential:

$$V_M(r \equiv |\mathbf{r_i} - \mathbf{r_{i+1}}|) = \begin{cases} D_0[e^{-2a_0(r-r_e)} - 2e^{-a_0(r-r_e)}] & r < r_c \\ a_s(r-r_c)^2 + b_s(r-r_c)^3 & r_c \leqslant r \leqslant r_c + \Delta, \\ 0 & r \geqslant r_c + \Delta \end{cases} \tag{2}$$

where D_0 is the potential well depth, r_e is the equilibrium bond length at rest, while a_0 determines the stiffness of individual bonds according to $V_M''(r_e) = 2a_0^2 D_0$. The bead-bead potential V_M is smoothly switched off in between r_c and $r_c + \Delta$ ($r_c \gg r_e$), with a_s and b_s uniquely determined by the request that $V_M(r)$ and $V_M'(r)$ are continuous everywhere.

Inspection of the $V_M'(r)$ derivative shows that a bond along the chain can withstand a static tension of at most $\tilde{f}_1 = (a_0 D_0)/2$ that is reached at positive elongation $\delta r = \log(2)/a_0$ from the minimum of the potential at an energy that is $D_0/4$ above the bottom of the potential well and $3D_0/4$ below the dissociation limit.

The system potential energy, therefore, is given by:

$$E\left[\mathbf{r_0^{(k)}}; \mathbf{r_i^{(k)}}; \mathbf{r_{N_b+1}^{(k)}} \middle| 1 \leqslant i \leqslant N_b; 1 \leqslant k \leqslant N_c\right] = \sum_{k=1}^{N_c} \left\{ \frac{1}{2} K_w \left|\mathbf{r_1^{(k)}} - \mathbf{r_0^{(k)}}\right|^2 + \sum_{i=1}^{N_b-1} V_M(|\mathbf{r_i} - \mathbf{r_{i+1}}|) + \frac{1}{2} K_w \left|\mathbf{r_{N_b}^{(k)}} - \mathbf{r_{N_b+1}^{(k)}}\right|^2 \right\}. \tag{3}$$

Each regular and end-point bead has mass m, and the system kinetic energy is

$$E_{\text{kin}} = \frac{1}{2} m \sum_{k=1}^{N_c} \sum_{i=0}^{N_b+1} \left|\dot{\mathbf{r}}_i^{(k)}\right|^2. \tag{4}$$

In what follows, it is assumed that the particle of index 0 of each chain is the end particle on the plane at $z = z_a$, while the particle of index $N_b + 1$ is the terminal bead at z_b.

According to these equations, particles on different chains interact with each other only through the clamps. This demands that the chains are widely separate or, equivalently, that their density is low. Moreover, even along the chain, only nearest-neighbor beads interact with each other, reflecting the predominantly 1D topology of polymeric fibers.

The z component of the force on each of the end points located on the plate at $z = z_a$ is given by:

$$f_0^{(k)} = K_w\left(z_1^{(k)} - z_a\right). \tag{5}$$

We want the total force on the plate to be F, i.e., the plate on the left will pull the bundle with a constant force $-F$:

$$F = K_w \sum_{k=1}^{N_c} \left(z_1^{(k)} - z_a\right) = K_w \left(\sum_{k=1}^{N_c} z_1^{(k)}\right) - N_c K_w z_a. \tag{6}$$

The constraint on the force, therefore, is identically satisfied if, at any given time, we set z_a to be

$$z_a = \frac{1}{N_c}\left[\left(\sum_{k=1}^{N_c} z_1^{(k)}\right) - F/K_w\right]. \tag{7}$$

Similar equations hold for the other side of the bundle, whose reference plane is $z = z_b$. In other terms, we treat the two plates as zero-mass objects, adjusting instantaneously to the force from the bundle, in such a way that the tension imposed from outside is constant.

In a series of preliminary simulations at $F = 0$ we observed that, as expected, the simulated sample forms an approximatively Gaussian coil. However, the equilibrium, separation of the two planar clamps at $z = z_a$ and $z = z_b$, is much shorter than the $\Delta_z = r_e\sqrt{N_b/3}$ end-to-end distance predicted by the Gaussian model for individual chains [29]. This somewhat unexpected observation is apparently due to the confinement of the end-chain beads on the two parallel planes at $z = z_a$ and $z = z_b$, and we verified that removing this constraint restores the Gaussian value for the end-to-end distance in each of the noninteracting chains. Moreover, the short separation of the clamps is apparently made possible by the absence of bead-bead and bead-clamp interactions that allows the two clamps to sit well within the blob, as regular beads can be found on either side of the $z = z_a$, $z = z_b$ planes.

Although intriguing, we did not analyze this short separation of the clamps in further detail, but considering that the original model did not provide a realistic representation of polymeric bundles joining two opposite surfaces, we slightly modified it to include a soft repulsive potential confining beads inside the portion of space delimited by the two parallel plates at $z = z_a$ and at $z = z_b$. The analytical expression of the added

potential is

$$U_{\rm soft} = \frac{1}{2}K_s \sum_{k=1}^{N_c}\sum_{i=2}^{N_b-1}\left[\phi_a\left(z_i^{(k)}\right)+\phi_b\left(z_i^{(k)}\right)\right], \tag{8}$$

where

$$\phi_a(z) = \begin{cases}(z-z_a)^2 & z < z_a \\ 0 & z \geqslant z_a\end{cases} \tag{9}$$

and

$$\phi_b(z) = \begin{cases}(z-z_b)^2 & z > z_b \\ 0 & z \leqslant z_b\end{cases}. \tag{10}$$

We do not include the contributions for particles 1 and particle N_b to avoid straining bonds that by necessity are located close to the boundary planes and are the most affected by any sudden displacement of these planes.

For the sake of simplicity, we set $K_s = K_w$. This represents a moderately repulsive potential that does not strictly prevent particles to enter the "external" portion of space, but it is certainly sufficient to drastically reduce the spill out of beads, thus enforcing the role of the plates as the exterior boundary of the simulated bundle.

Upon adding the soft-wall potential, the $(z_b - z_a)$ separation increases beyond the Gaussian chain end-to-end separation $\Delta_z = r_e\sqrt{N_b/3}$ because of the inside pressure exerted by the particle on the boundary walls. The wall-bead interaction is included in the computation of the stress on the z_a, z_b boundary planes. Because of the piecewise definition of the two functions $\phi_a(z)$, $\phi_b(z)$ at $z = z_a$ and $z = z_b$, the relation between F and z_a or z_b can no longer be solved analytically, but a simple iteration scheme achieves convergence within a few steps.

To prevent the breaking of bonds during the long runs that are needed to equilibrate our samples, a confining potential has been added to every pair of interacting particles:

$$V_{\rm conf}(|\mathbf{r_i}-\mathbf{r_{i+1}}|) = \begin{cases}0 & |\mathbf{r_i}-\mathbf{r_{i+1}}| \leqslant R_{\rm conf} \\ \frac{1}{2}k_{\rm conf}(|\mathbf{r_i}-\mathbf{r_{i+1}}|-R_{\rm conf})^2 & |\mathbf{r_i}-\mathbf{r_{i+1}}| > R_{\rm conf}\end{cases}. \tag{11}$$

A nonvanishing $k_{\rm conf}$ force constant will be used for equilibration and set smoothly to zero at the beginning of the production stage of our simulations, opening the way to the breaking of bonds.

Most of the computational time is required to evaluate the Morse potential between nearest-neighbor beads. In comparison, the iterative determination of the z_a, z_b coordinates of the end blocks requires negligible effort.

The majority of our simulations have been carried out at constant temperature conditions, coupling all beads to a Langevin thermostat, implemented according to the prescriptions of Ref. [30]. Newton's equations of motion are replaced by the Langevin expression:

$$\dot{\mathbf{r}}_\mathbf{i} = \mathbf{v_i}, \tag{12}$$

$$m\dot{\mathbf{v}}_\mathbf{i} = \mathbf{f_i} - \eta\mathbf{v_i} + \beta_\mathbf{i}(t), \tag{13}$$

where f_i are the forces derived from the potential energy, η is the friction coefficient, while $\beta_\mathbf{i}$ are random forces, satisfying the relations:

$$\langle\beta_\mathbf{i}(t)\rangle = 0, \tag{14}$$

$$\langle\beta_\mathbf{i}(t)\beta_\mathbf{j}(t')\rangle = 6\eta k_B T\delta_{i,j}\delta(t-t'). \tag{15}$$

In these last relations, k_B is the Boltzmann constant and T is the target temperature of the simulation. In our computer code, we faithfully implemented Eq. (18) and Eq. (21) to Eq. (23) of Ref. [30], slightly modifying the velocity Verlet algorithm used in the $\eta = 0$ case. In our choice of units, $k_B = 1$, and temperature is measured in energy units.

To assess the role of the Langevin thermostat and dynamics, a series of simulations have been carried out upon disconnecting particles from the thermal bath, i.e., setting $\eta = 0$ and excluding random forces. As mentioned in the Introduction, the Langevin simulations correspond to systems in a thermally conducting environment such as a solution, while simulations at $\eta = 0$ approach the condition of experiments in which polymeric bundles are broken at high speed [31].

Because of the relatively large number of parameters, it might be useful to provide an overview of their role. D_0, r_e, and a_0 determine the Morse portion of the nearest-neighbor bead-bead potential, representing energy, length, and elastic spring constant of nearest-neighbor (covalent) bonds along the polymer backbone. The bead-bead potential has finite range vanishing beyond $r_c + \Delta$ and starts to deviate from the Morse function for $r > r_c$. Both r_c and Δ are auxiliary parameters, whose choice ($r_e \gg r_e$, $\Delta/r_e < 1$) ideally should not affect significantly the result of the simulation. The link from the first and last bead to the clamps is harmonic (force constant K_w), and a piecewise continuous, harmonic potential of force constant K_s has been added to (softly) confine beads in between the clamps. The K_w and K_s values have been set fairly low to ease the iterative solution of the equations for z_a and z_b. Since the force acting between the clamps and the bundle is fixed from the outset, the choice of K_w and K_s does not affect the results. Selecting a stiffer force constant would be equivalent to somewhat displace inwards the clamps. The confining potential $V_{\rm conf}$ [Eq. (11)] is a transient feature of our model, used only during equilibration to prevent the untimely breaking of bonds. Once again, its parameters are meant to influence the result as little as possible.

It would be tempting to see the limiting force $\tilde{f}_1 = (a_0 D_0)/2$ that can be sustained by individual bonds as a natural scale of force on single chains [$\tilde{F}_1 = (N_c a_0 D_0)/2$ on bundles]. This force, however, is sufficient to break each chain almost instantaneously and is therefore one order of magnitude higher than the loads considered in our simulations that concern instead thermally activated creep. Because of this, our results are not a unique function of $F/\tilde{F}_1$.

At equilibrium, temperature and energy scale D_0 would not be independent variables, and all average results would depend on D_0/T only. Under nonequilibrium conditions, this is not strictly true, but the conditions of our simulations are never far from short-term equilibration, and we verified that fast relaxing properties (time-dependent energies and energy fluctuations, for instance) are indeed functions of D_0/T. We anticipate that the irreversible kinetics of our system is primarily activated,

hence the rate of events such as bond and chain breaking follows an Arrhenius law, i.e., they scale like $\exp[-\Delta/T]$, where Δ is the activation free energy for the event under consideration, which, to first order, is expected to scale like $\sim D_0$.

At zero applied force, and excluding the thermostat (i.e., $\eta = 0$), energy is conserved. We verified that even in the $\eta = 0$ case, the interchain coupling through the leads is sufficient for an effective equilibration among chains. On the other hand, when $\eta > 0$ and $F = 0$, the sample temperature equilibrates at the set temperature T on a time scale that depends on the η value.

The fiber bundle model is sometimes applied to the investigation of soft fibrous materials such as paper or wood. The structure and local properties of these systems are characterized by quenched disorder, whose amplitude and distribution affect the creep evolution through the formation of weak links. Polymeric samples, instead, are far more homogeneous, and our model accounts only for annealed disorder, due to a nonvanishing temperature of the sample during the creep simulation. Quenched disorder, however, could easily be reintroduced by considering a statistical distribution of the potential well depth D_0 [see Eq. (2)] attributed to individual bonds.

We remark that neglecting general bead-bead interactions besides the *covalent* bonds along the chain is the major approximation introduced in our model that has the merit of drastically reducing the computational cost of our study. More importantly, it has also the advantage of retaining a close relation between our approach and the classical fiber bundle model. Last but not least, our model could indeed represent real systems, consisting of polymeric fibers in solution at the Θ point [29].

III. RESULTS

For the sake of clarity, before presenting the results we summarize here the notation that is used throughout the paper. Simulated samples consist of fibers (chains), each made of beads. The number of chains and of beads per chain are N_c and N_b, respectively. At any given time, the number of intact chains is $n_c(t)$, while the number of broken chains and broken bonds are $n_{bc}(t)$ and $n_{bb}(t)$, respectively. The total load on the bundle is F, and the initial load per chain is $f_1 = F/N_c$. The load on intact chains increases with increasing damage of the bundle, and this will be denoted by $f_1(t) = F/[N_c - n_{bc}(t)]$. The average lifetime of bundles subject to the same load F is denoted by τ, while the breaking time of the individual bundle j is τ_j.

The process of breaking single anharmonic chains similar to those considered in our study has been investigated a few times in the past [26–28] using molecular dynamics simulations. At nonvanishing temperature, the breaking rate of such chains under constant tension f_1 follows the Arrhenius law of activated processes, with an activation energy that decreases linearly with increasing applied tension f_1. The chain lifetime scales with its length N according to $N^{-\beta}$, with $0 < \beta < 1$. The exponent β approaches 1 with $f_1 \to 0$, and slowly tends to zero with increasing f_1. These conclusions are based on the results of constant temperature simulations, at temperatures T and applied tensions f_1 that are relatively high compared to those used in our study [26–28]. Despite the slight differences in the model and in the simulation parameters, these results of Ref. [26–28] provide the first basic elements to interpret our data.

TABLE I. Parameters entering the definition of the model potential. The mass of each particle is set to $m = 1$.

D_0	r_e	a_0	r_c	Δ	K_w	K_s
6	1.5	2	3	0.5	0.2	0.2

A. System and simulation setup

Most of our simulations have been carried out for bundles of $N_c = 400$ chains, each consisting of $N_b = 100$ beads. The parameters of the model potential are listed in Table I. Recombination of broken bonds is not allowed, but the effect of bond recombination has been investigated by a few test computations, whose results are summarized in Sec. III D.

In a first stage of our investigation we prepared a library of 200 starting configurations, equilibrated at the reduced temperature $T = 0.33$. Equilibration has been carried out under a moderate tensile load $F = 5$, introduced to keep $z_b > z_a$, and to limit fluctuations in the length of the bundle. To test the stability of our MD code and our choice of the simulation parameters, equilibration has been carried out upon disconnecting the sample from the thermal bath [$\eta = 0$ in Eq. (13)] that otherwise could conceal the drift of temperature and potential energy. Moreover, to prevent the breaking of bonds during this preliminary stage, the confining potential described in Eq. (11) has been included with $R_{\rm conf} = 0.6$, $k_{\rm conf} = 0.4$. Under these conditions, a sample has been equilibrated for 50×10^6 steps, with occasional (small) rescaling of velocities to set the temperature. Then we carried out a MD simulation lasting 200×10^6 steps, selecting and storing one configuration every 10^6 steps. In the units implicitly defined in Table I, the time step used in all of our simulations is $\delta t = 0.025$. The computation takes about 1 h for 10^6 MD steps on a single x86_64 core running at 2.80 MHz.

At this stage, before introducing bond and chain breaking mechanisms, the system behaves like a (slightly visco)-elastic polymeric material, whose response to small-amplitude, long-wavelength perturbations consists of weakly damped oscillations. At very low T and under moderate tension, the speed of sound is easily computed from the phonon dispersion relation of monoatomic harmonic chains [see Ref. [32], Eq. 22.31, p. 433] $c_s = \sqrt{V_M''(r_e)/m}$, where $V_M(r)$ is the Morse potential of Eq. (2) and $m = 1$ is the mass of each bead, giving $c_s = a_0\sqrt{(2D_0)} \approx 7$ in our units of length and time. At the temperature ($T = 0.33$) of our simulations, however, the relevant forces stabilising the Gaussian coil configuration are of entropic origin [29], and the bundle behaves like a 1D elastic system of spring constant $Y = 3k_BT/N_br_e^2$ and linear density $\rho \sim N_b^{1/2}$ as predicted by the Gaussian theory of harmonic chains. Then the sound velocity is reduced to $c_s = \sqrt{Y/\rho} \sim 0.25$ (again for our systems and in our units). Following these considerations, it is easy to estimate a time

scale for the spontaneous oscillations of bundles, which turns out to be $\sim 10^2$ time units, as confirmed fairly accurately by our simulations. We do not have a simple model to predict the relaxation time of bundle oscillations due to the interaction among chains through the clamps. However, direct testing by MD shows that induced oscillations remain recognizable in the fluctuating noise of the bundle dynamics for about 10 full oscillations (10^3 time units), implying a relaxation time of a few (two or three) hundred time units. Thus, each chain as well as each bundle behaves like a weakly damped Kelvin-Voight element, already extensively used in the development of fiber bundle models [33].

For each sample, the production stage is initiated by smoothly removing the confining potential and bringing the external load to the intended value $F = f_1 \times N_c$, according to:

$$k_{\rm conf}(t) = \begin{cases} k_{\rm conf}^{\rm (eq)} - \frac{1}{2}k_{\rm conf}^{\rm (eq)}\left\{1+\cos\left[\pi\left(1+\frac{t}{t_{\rm sm}}\right)\right]\right\} & t < t_{\rm sm} \\ 0 & t > t_{\rm sm} \end{cases} \tag{16}$$

$$F(t) = \begin{cases} F_{\rm eq} + \frac{1}{2}(F - F_{\rm eq})\left\{1+\cos\left[\pi\left(1+\frac{t}{t_{\rm sm}}\right)\right]\right\} & t < t_{\rm sm} \\ F & t > t_{\rm sm} \end{cases} \tag{17}$$

where the smoothing time is set to $t_{\rm sm} = 2500$, while $k_{\rm conf}^{\rm (eq)} = 0.4$, $F_{\rm eq} = 5$ are the strength of the confining potential and the low tension applied during equilibration, respectively. The continuous change of $k_{\rm conf}$ and F from their equilibration to production values has been devised to prevent the early breaking of chain due to the sudden change of forces on the particles in our samples.

B. Results of simulations based on the Langevin dynamics

We report first the results of the constant temperature simulations, enforced through a Langevin thermostat with $T = 0.33$ and $\eta = 0.0001$, whose aim is to remove the excess heat generated by the work done by the external force and to replenish the energy dissipated through the irreversible breaking of bonds. The low value of η, in particular, has been selected to retain the fluctuations in forces, velocities, and displacements that follow the breaking of each chain that are essential features in the behavior of these systems and processes.

Simulations have been carried out at 13 values of the applied tension $0 \leqslant F \leqslant 100$. More precisely, 20 bundles have been simulated for each of the loads: $F = 0, 5, 10, 15, 30, 50, 60, 70, 80, 90$; 50 bundles have been simulated at $F = 20$, $F = 100$, and 200 bundles at $F = 40$.

In all cases, including $F = 0$, removing the confining potential causes the progressive breaking of bonds, that, in the absence of recombination, proceeds irreversibly, accompanied by the progressive increase of the bundle length (see Fig. 1). In the early stages of our simulations, bond breaking events appear to be independent of each other, taking place by thermal fluctuations at a nearly constant rate αN_c (α being the bond breaking rate per chain, see Fig. 2), which depends primarily on the sample temperature [34] and, more weakly, on the applied tension (see the inset of Fig. 2). The progressive accumulation of damage due to this random process represents the microscopic origin of the bundle ageing that in several

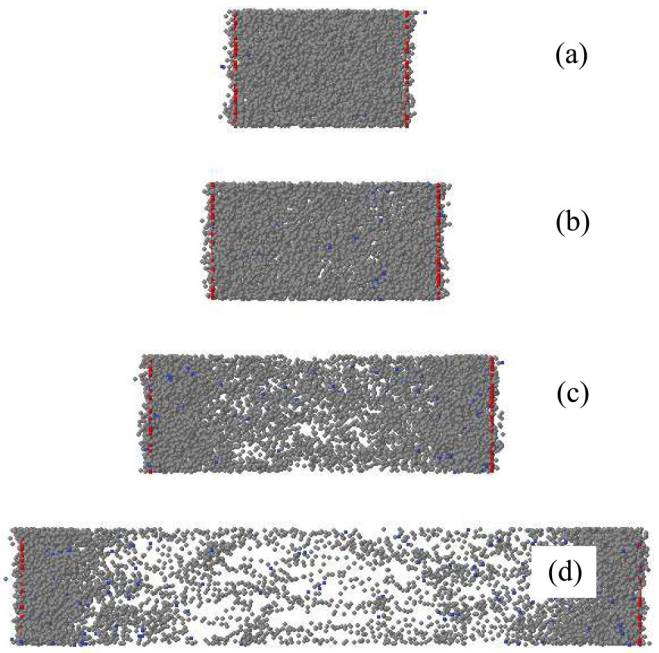

FIG. 1. (Color online) Snapshots from a simulation at $T = 0.33$, $F = 40$. Black particles: Regular beads, twofold coordinated; blue particles: onefold coordinated beads, marking broken bonds; red particles: chain terminations on the $z = z_a$ and $z = z_b$ planes. For the sake of clarity, only 1/4 of the chains are displayed. (a) $t/\tau_i = 0.025$; (b) $t/\tau_i = 0.5$; (c) $t/\tau_i = 0.66$; (d) $t/\tau_i = 0.975$.

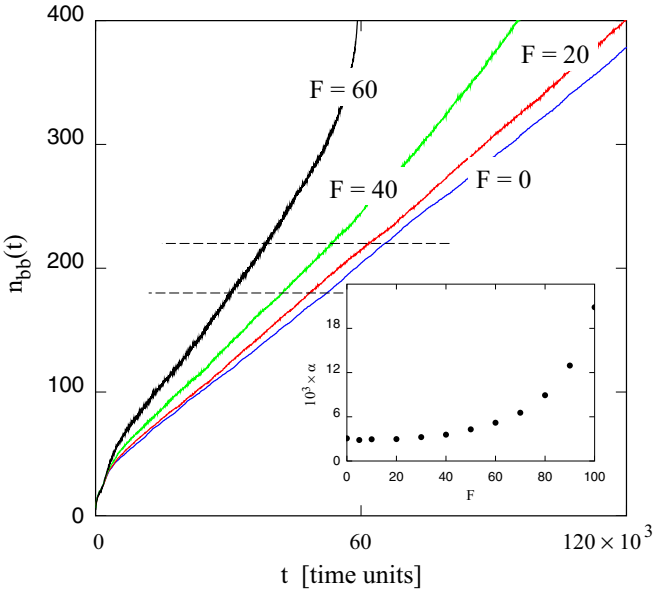

FIG. 2. (Color online) Average number of broken bonds as a function of simulation time in samples at $T = 0.33$, $F = 0$, 20, 40 and 60. Inset: Slope of the linear portion of $n_{bb}(t)$, estimated by linear fit of the $180 \leqslant n_{bb}(t) \leqslant 220$ range. The range of the linear fit is delimited by the two horizontal dashed lines in the main plot. Results averaged over all the samples simulated at the same load, see text.

models is accounted for through suitable phenomenological coefficients [35]. In the latest stages, the rate of bond breaking increases significantly, reflecting the concentration of stress on the chains that still connect the two end planes. To within statistical accuracy, at all times broken bonds are uniformly distributed along the entire length of the polymeric chains. The pile-up of particles in close proximity of the clamps that can be seen in Figs. 1(c) and 1(d) is due to broken chains that fold into a nearly Gaussian coil, only slightly perturbed by the soft external wall.

At first, each bond breaking is likely to break a chain, and thus:

$$\frac{dn_{bc}(t)}{dt} = \alpha N_c, \tag{18}$$

where, as already stated, α is the rate of bond breaking per chain. With increasing damage of the bundle, it increases also the probability that a bond breaking event occurs on a chain that is already broken. In this way, the rate of chain breaking is decoupled from the bond breaking rate, and, in particular, the chain breaking rate can decrease well below the rate αN_c of bond breaking. Eventually, this purely statistical effect would reduce the rate of chain breaking to just $1/N_c$ of the initial rate. However, this reduction is to some extent offset by a mechanical effect, since the decreasing number of intact chains increases the average tension that each of these chains has to withstand. This, in turn, increases the rate of chain breaking, according to the effect quantified in Refs. [26–28] and reproduced by our computations (see inset in Fig. 2). At variance from the first, the second effect is purely due to the chain-chain interaction through the end blocks, and its detailed effect depends on the load-sharing mechanism adopted by the model.

The competition of these two effects is apparent in the time dependence of the number of broken chains that is shown in Fig. 3 for three values of the applied stress. Despite their spanning fairly different time scales, all the curves share a few general aspects. Apart from the first 2500 time units, affected

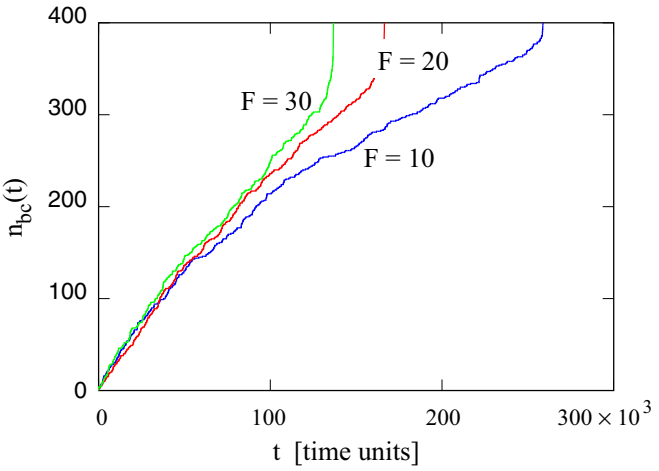

FIG. 3. (Color online) Number of broken chains as a function of simulation time in individual samples at $T = 0.33$ under the tensile load $F = 10$, $F = 20$, $F = 30$. No averaging has been carried out in this case.

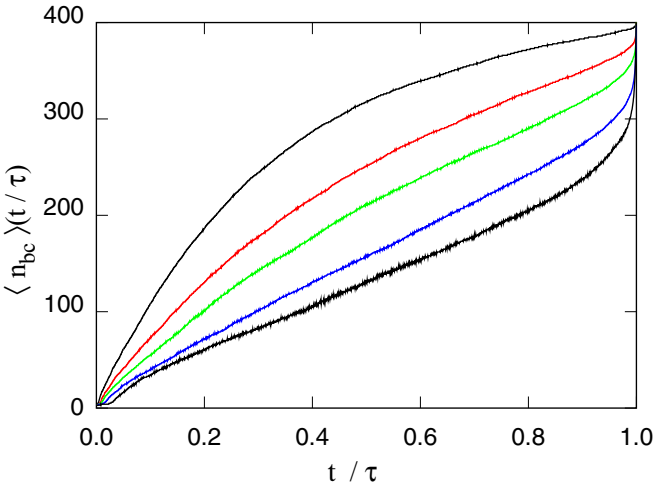

FIG. 4. (Color online) Number of broken chains as a function of scaled time at five values of the tensile load F. τ_i is the time to break individual bundles, see text. The results have been averaged over all the samples under the same tensile load. From top to bottom: $F = 0$, 10, 20, 40, 60.

by the change of F and by the switch off of the confining potential, a first stage of rapid raise in the number of broken chains is followed by an almost linear range, turning into a final avalanche of chain breaking events that completes the failing process.

A visual summary of these results is obtained by first plotting the $n_{bc}(t)$ curve for each bundle j as a function of t/τ_j, where τ_j is the breaking time of that individual sample. Then, all the curves for a given value of F, that now span the same $0 \leqslant t/\tau \leqslant 1$ domain, are averaged. In other terms, we compute and plot the function:

$$\beta(u) = \langle n_{bc}(u\tau_i) \rangle_i, \tag{19}$$

where $0 \leqslant u \leqslant 1$, and the average is over all possible initial conditions for the intact bundle at $T = 0.33$. For the sake of simplicity, we shall use the loose notation $\langle n_{bc} \rangle (t/\tau)$ for $\beta(u)$ and for similar elaborations of other properties such as the bundle length.

The results for $\langle n_{bc} \rangle (t/\tau)$ are displayed in Fig. 4, showing that in the *regular* $0.2 \leqslant t/\tau \leqslant 0.8$ range, the decrease of the chain breaking rate with increasing time is more pronounced at low F load, while, as expected, the size and relative duration of the avalanche stage are higher at high values of F.

While the avalanche stage is difficult to predict and to describe, the early stages of creep progression can be modelled on the basis of the few considerations listed in the previous paragraphs. To first approximation, let us assume that the rate of bond breaking is constant:

$$\frac{dn_{bb}(t)}{dt} = \alpha N_c \tag{20}$$

and each bond breaking event has a probability:

$$P(t) = \frac{[N_c - n_{bc}(t)]}{N_c} \tag{21}$$

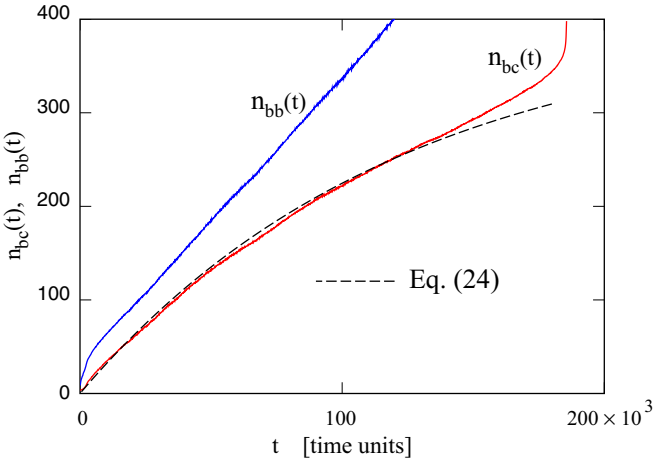

FIG. 5. (Color online) Number of broken bonds and of broken chains as a function of time in a sample at $T = 0.33$ under load $F = 20$. The full line is the prediction of Eq. (23) in the text.

to break an intact chain. Then the rate of chain breaking is

$$\frac{dn_{bc}(t)}{dt} = \alpha N_c \frac{[N_c - n_{bc}(t)]}{N_c}, \tag{22}$$

whose solution is

$$n_{bc}(t) = N_c[1 - \exp(-\alpha t)], \tag{23}$$

where the constant rate α is estimated from the central portion of the broken bonds versus time curves, Fig. 2.

Comparison of this prediction for $n_{bc}(t)$ with the results of the computational experiment reveals a fair agreement for most of the $n_{bc}(t)$ curve, up to the beginning of the final avalanche (see Fig. 5). The final avalanche is caused by the fact that with increasing bundle damage the load on each of the intact chains increases. This makes it more likely to break bonds on the intact rather than on broken chains and, perhaps more importantly, it enhances the cooperativity of the intact chains evolution, eventually triggering avalanches. This simple picture allows us to define the avalanche, as the portion of the $n_{bc}(t)$ deviating from the predictions of Eq. (23).

To this aim, we compute the numerical derivative of the $n_{bc}(t)$ curves shown in Fig. 4 that represents a time dependent rate of breaking chains. We identify the beginning of the final avalanche with the time t_{av} at which this time-dependent rate equals 2 times the average breaking rate N_c/τ. In this way, we determine the portion of the lifetime and of the bundle damage that is accounted for by the last stage of avalanche failing. The results are summarized in Fig. 6. The transition from secondary creep to avalanche is fairly sharp, and therefore the results do not depend significantly on the precise value of the threshold rate chosen to define t_{av}. Up to the highest load explored in our simulations, the avalanche stage does not exceed ~15% of the bundle lifetime but accounts for up to ~50% of the chain breaking events (see the inset in Fig. 6).

The avalanche stage is marked by strong correlations in breaking times, since the failing of even a single chain triggers further breaking events. This is illustrated in Fig. 7, where we show the probability distribution for the time between successive chain breaking events, separating the first and

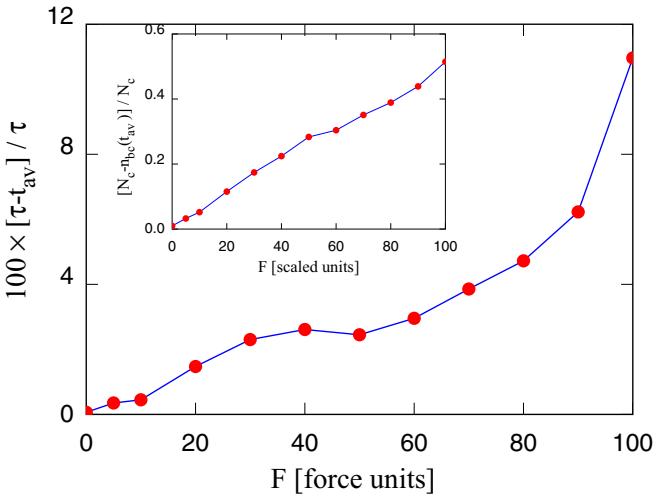

FIG. 6. (Color online) Relative fraction of the bundle lifetime accounted for by the avalanche stage. The avalanche starts at t_{av}, defined as the time at which the time dependent rate of chain breaking equals two times the average rate N_c/τ. Inset: Fraction of chains in the bundle that break during the avalanche stage.

second half of the entire bundle simulation. In the first case, the probability distribution is very broad and nearly structureless. In the second half of the simulation, a narrow peak at low times results from the rapid chain collapse during the avalanche stage.

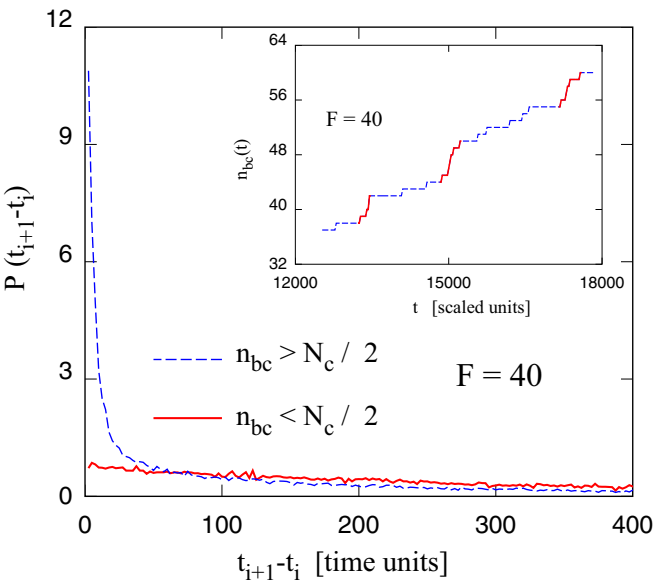

FIG. 7. (Color online) Probability distribution $P(\delta t)$ for the time interval between two successive chain breaking events. The red curve refers to events taking place when the number of broken chains is less than 50%, and the blue dashed curve refers to the remaining 50% of chain breaking events and includes the effect of the final avalanche. Average over 200 bundles of $N_c = 400$ chains of $N_b = 100$ at $T = 0.33$ under load $F = 40$. Inset: Detail of $n_{bc}(t)$ for a single bundle at $T = 0.33$ under load $F = 40$ in the early stages of stretching. Short bursts of correlated chain breaking events are shown in red (full line), while regular steady segments are shown in blue (dashed line).

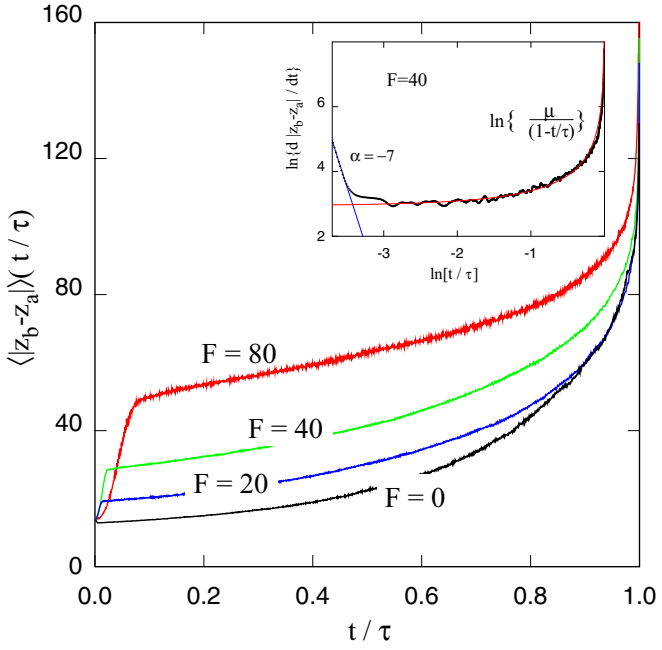

FIG. 8. (Color online) Bundle elongation as a function of time at four values of the tensile load. Data in the main panel have been scaled and averaged as in Fig. 4. From bottom to top: $F = 0, 20, 40, 80$. Inset: Logarithmic plot of the strain rate $\dot{\gamma}(t) = d|z_b - z_a|/dt$ for bundles at $T = 0.33$ and $F = 40$. Dots: Simulation data. Straight line (blue): Linear interpolation of the $0 \leqslant t/\tau \leqslant 0.027$ data, corresponding to a power-law dependence $\dot{\gamma}(t) \sim t^{-\alpha}$; red curve: Interpolation of the $0.95 \leqslant t/\tau < 1.0$ data with a polelike term $\dot{\gamma}(t) \sim \mu/(1 - t/\tau)$ diverging at $t = \tau$.

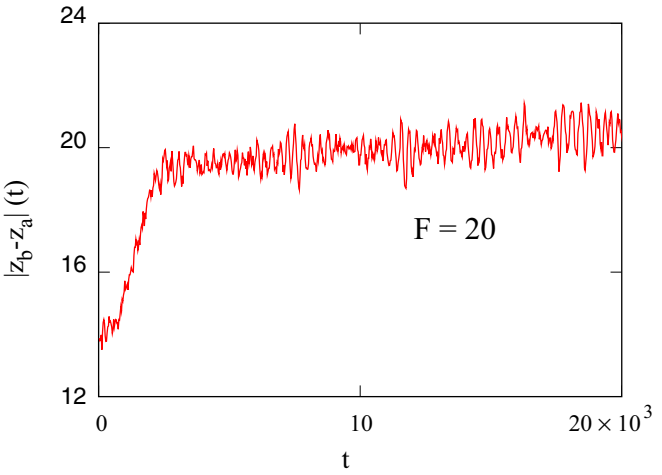

FIG. 9. (Color online) Bundle elongation as a function of time at tensile load $F = 20$. Results refer to a single bundles; no averaging over samples has been carried out.

In many respects, the information contained in Fig. 7 is relatively trivial, since it mainly reflects the global quickening of the bundle kinetics towards the end of its lifetime, without highlighting special correlations or cause-effect relations among the events. Perhaps more telling are bursts of chain breaking that develop already in the early stages of our bundle breaking simulations (see inset in Fig. 7) and represent the most obvious precursors of the final avalanche. These bursts are apparent from the visual impression of $n_{bc}(t)$ curves for single bundles but are difficult to unambiguously define and quantify. More importantly, our simulations do not provide sufficient statistics to investigate the properties of these bursts.

The results for the time dependence of broken bonds and chains are reflected in the parallel evolution of the bundles' length $L_z(t) \equiv |z_b - z_a|(t)$ [36] that is illustrated in Fig. 8. The simulation data in this figure have been treated as in Fig. 4, representing in fact $\langle L_z \rangle(t/\tau)$. The bundle length changes rapidly at first when the load is applied, with superimposed oscillations of fairly small amplitude and period of the order of 100 time units (see Fig. 9) not seen in Fig. 8 because of averaging over multiple samples but apparent in the results for individual bundles. Then the bundle length raises nearly linearly, up to the point at which the last avalanche stage begins, marked by an increasing upwards curvature of $\langle L_z \rangle$ versus time. Small-amplitude oscillations at the frequency of the bundle (quasi)-eigenmodes continue throughout the simulation, excited by the sudden changes in the end-wall position caused by chain breaking events and continuously damped by the complex many-particle dynamics of our samples. These damped oscillations provide a simple representation of creep ringing observed in experiments and discussed in a number of papers [37].

Experimental data are often presented and discussed in terms of the time-dependent strain rate $\dot{\gamma}(t) = d[\langle L_z \rangle(t/\tau)]/dt$. The logarithmic plot of $\dot{\gamma}(t)$ versus time displays three characteristic stages, identified as the primary, secondary, and tertiary regimes of creep [38,39] well known from the technological characterization of materials. The first stage, also known as Andrade creep [40], is characterized by a power-law dependence of the strain rate on time $\dot{\gamma}(t) \sim t^{-\alpha}$, whose exponent α, in soft fibrous materials, is typically close to unity [25] and can be derived from the viscoelastic properties of the sample [41,42]. The secondary regime is marked by a minimum of $\dot{\gamma}(t)$, occurring at the *universal* value of the scaled time $t_{\min}/\tau = 0.556$ [43], while the third regime corresponds to the avalanche stage, with an apparent divergence of the strain rate at the time $t = \tau_j$ of the bundle breaking. As a result of these observations, the entire plot for the strain rate $\dot{\gamma}(t)$ can be approximated by the simple expression:

$$\dot{\gamma}(t) = \lambda \left(\frac{t}{\tau} \right)^{-\alpha} + \frac{\mu}{1 - t/\tau} \tag{24}$$

(see Eq. (1) in Ref. [25]).

To compare with these experimental observations, we report on a logarithmic scale the time dependence of the strain rate averaged on our 200 simulations at $F = 40$ (see the inset in Fig. 8). The result has an obvious qualitative correspondence with the experimental picture, with, however, quantitative differences that might be considered equally or even more important than the similarities. First, it is certainly true that the expression of Eq. (24) provides an excellent fit of our strain rate data, but the exponent α turns out to be very high ($\alpha \sim 7$) compared to the values around unity found by measurements on soft fibrous materials. As a consequence, the $\dot{\gamma}$ valley turns out to be very broad, and the absolute minimum is difficult to accurately identify but seems to be located at

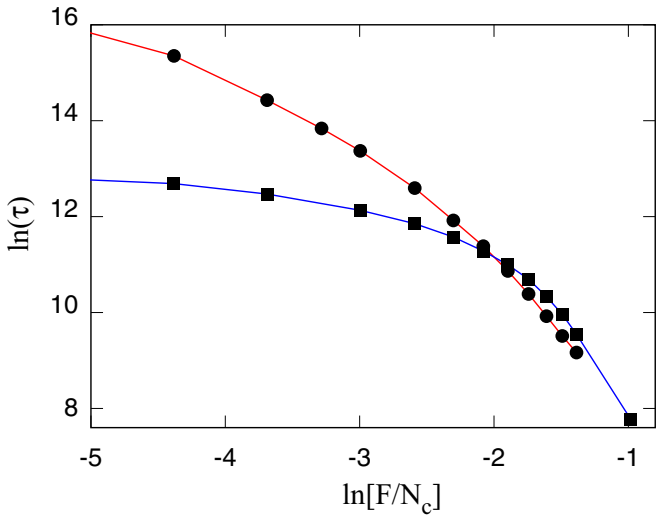

FIG. 10. (Color online) Lifetime of fiber bundles as a function of the tensile load. Filled squares: Constant temperature simulations with a Langevin thermostat at $T = 0.33$ and $\eta = 0.0001$. Full dots: Newtonian simulations (no friction and no random forces) started from samples equilibrated at $T = 0.33$. Blue and red lines are a guide to the eye.

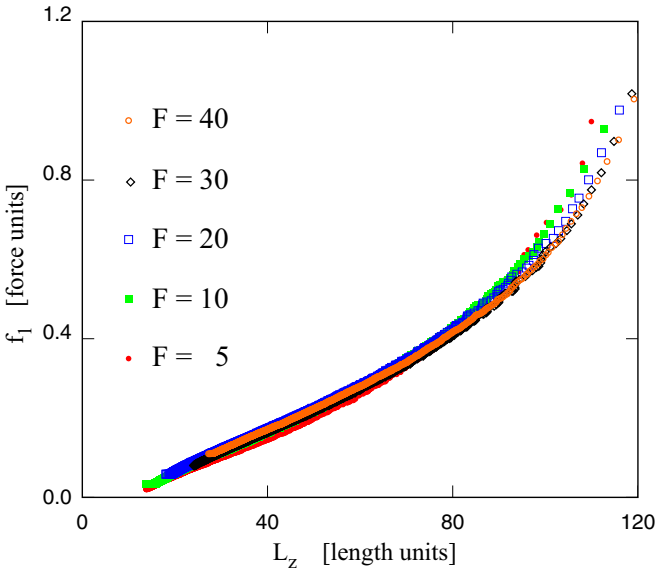

FIG. 11. (Color online) Stress f_1 versus bundle length L_z in samples under load F from 5 to 40. The definition of f_1 contains an extra term accounting for the internal pressure of the bundles, see Eq. (26).

$t/\tau \sim 0.12$, well before the *universal* value $t_{\min}/\tau = 0.556$ already mentioned in the previous paragraph. We think that the quantitative discrepancy on the α exponent and on $t_{\min}/\tau$ is due to our specific way to apply the load and to remove the confining potential according to Eqs. (16) and (17) with a relatively short $t_{\rm sm}$. The extreme microscopic size of our samples, the harmonic bond at the chain-clamp junction, the ideal rigidity of the clamps, and the absence of general bead-bead interactions might play a complementary role.

As expected, the lifetime of bundles decreases rapidly with increasing tensile load. The logarithmic plot of τ versus F shown in Fig. 10 displays a marked curvature, ruling out a simple scaling law such as:

$$\tau = F^{-\gamma}, \quad \gamma > 0 \tag{25}$$

over the entire range of F. On the low-tension side, this result is to be expected, since the finite lifetime of all our samples excludes a divergent prediction such as given by Eq. (25) in the $F \longrightarrow 0$ limit. On the high-tension side, however, the logarithmic plot of τ versus F approaches a linear behavior with a slope of -3.9. Taking into account the transient time needed to switch on the load, the exponent becomes -4 to within the small error bar, thus giving $\tau \sim F^{-4}$ in the high-load regime.

The same power-law dependence, with a similar exponent, has been found in the experimental characterization of creep failure in protein gels [25]. The good correspondence might be partly accidental, since our polymeric samples do not seem to have much in common with protein gels. Perhaps more relevant is the similarity with the lifetime versus load relation in the fatigue failing of fibrous materials such as paper and wood [44], generally described as one of the many instances of Basquin's law [45]. Needless to say, creep and fatigue are distinct phenomena, the first referring to static load and the second concerning time-dependent, cyclic loads. In our simulations, however, the distinction between static and time-dependent properties is somewhat blurred by the relatively short duration of the breaking process, and recovering the $\tau \sim F^{-4}$ behavior in the high load limit might be more than a mere coincidence.

It is tempting to speculate that, apart thermal fluctuations, the bundle length L_z and the effective stress on chains $f_1(t) = F/[N_c - n_{bc}(t)]$ are related by an equation of state $L_z[f_1]$ that depends on the system temperature but not on the total applied load F. The results of our simulations show that this assumption is justified only at a rather low order of approximation, since the $L_z[f_1]$ relations obtained at different F values overlap fairly closely but not exactly. Somewhat surprisingly, the largest deviation among curves occurs at low values of F, suggesting that the missing ingredient is the internal pressure due to the beads interaction with the confining potential. We verified that modifying the expression of the effective stress into

$$f_1 = \frac{(F + F_0)}{[N_c - n_{bc}(t)]} \tag{26}$$

with $F_0 = 2$ significantly improves the collapse of the different $L_z[f_1]$ data, as shown in Fig. 11. An even better result is obtained upon taking into account that the internal pressure decreases with increasing separation of the confining walls, replacing F_0 in Eq. (26) by $\tilde{F}_0/L_z$, but we did not carry out a systematic study of all physically motivated forms.

The general picture of creep provided by our simulations depends significantly on the ratio of the well depth of the Morse bead-bead potential ($D_0 = 6$ in the present computations) and simulation temperature ($T = 0.33$). A short series of simulations again at $T = 0.33$ with D_0 increased from 6 to 7 allowed us to verify that increasing the ratio of D_0 and T exponentially extends the bonds and chains lifetime,

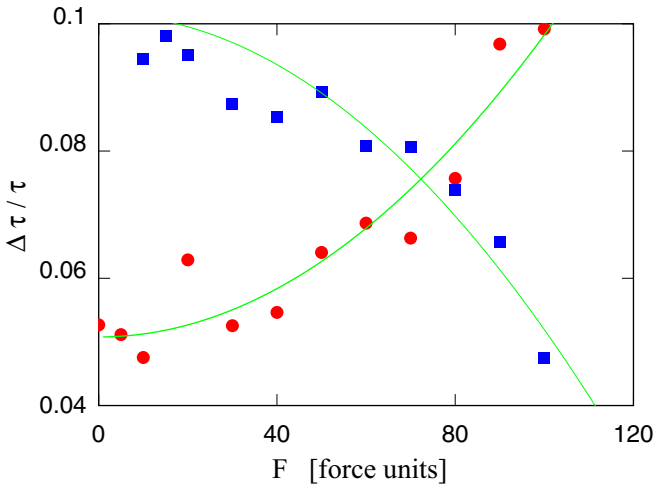

FIG. 12. (Color online) Relative uncertainty on the bundle lifetime τ as a function of the tension on the bundle. $\Delta\tau$ is the standard deviation of breaking times. Red dots: Langevin simulation; blue squares: Newtonian simulation. The continuous lines are quadratic fits to the simulation data given as a guide to the eye.

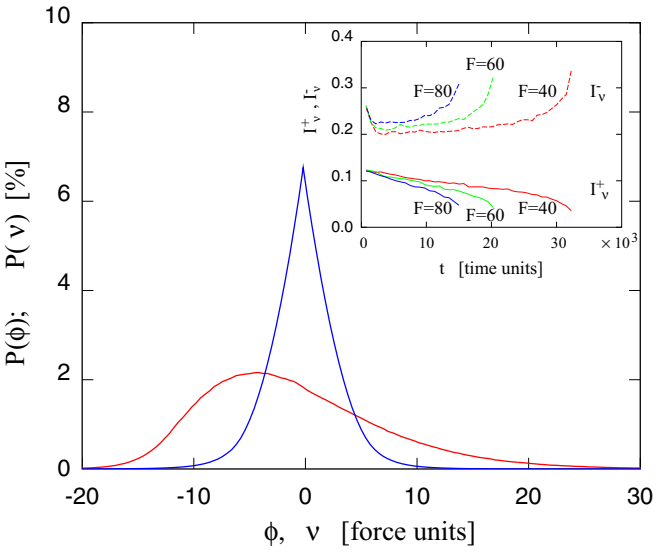

FIG. 13. (Color online) Probability distribution of the stress parameters ϕ (red line) and ν (blue line) on bonds in a sample under load $F = 20$. ϕ is the component of the force $\mathbf{F_{i+1}} - \mathbf{F_i}$ on the $(i,i+1)$ bond directed along the $\mathbf{r_{i-1}} - \mathbf{r_i}$ direction. ν is defined in a similar way but excludes the contribution from the direct $(i,i+1)$ interaction. Inset: Integral parameters I_ν^+ and I_ν^- [see Eq. (29)] as a function of time for three different values of the applied load. I^+ and I^- represent the fraction (in percentages) of bonds whose ν parameter exceeds the threshold value ($\nu^+ > a_0 D_0$; $\nu_- < -a_0 D_0$) for bond breaking (see text).

consistently with the Arrhenius theory of activated processes. The stabilization of bundles at high load with increasing D_0/T expands the linear range on the high-load side of the logarithmic plot in Fig. 10 and approaches more closely the picture provided by experimental measurements. Needless to say, the cost of simulations also increases exponentially with D_0/T, rapidly exceeding the available computer power.

Because of thermal fluctuations, and, even more, because of the unpredictable discharge of avalanches, the breaking time is a random variable, whose distribution is approximatively Gaussian. Even in the $F = 40$ case, for which 200 independent samples have been simulated, our statistics is insufficient to verify whether the probability distribution is indeed Gaussian or whether it is symmetric or slightly skewed.

The relative fluctuation in the breaking time is a parameter of obvious interest for applications. We found that the relative uncertainty ($\Delta\tau/\tau$, where $\Delta\tau$ is the standard deviation of the breaking times) is lowest at $F = 0$ and increases nearly quadratically with increasing applied load (see Fig. 12). This result is somewhat surprising, since one could think that applying an external perturbation would drive the system towards its fate reducing the role of fluctuations. The increase of $\Delta\tau/\tau$ with increasing F points to the important role of the final avalanche in enhancing the relative lifetime uncertainty at high F. We anticipate that the result differs when simulations are based on Newton's equation of motion, as discussed in Sec. III C.

To analyze the (im-)balance of forces that determine the irreversible deformation and eventual breaking of the sample, we monitor, first, the distribution of axial forces on each bond, defined as:

$$\phi_i = \ddot{d}_{i,i+1} = (\mathbf{F_{i+1}} - \mathbf{F_i}) \cdot \frac{(\mathbf{r_{i+1}} - \mathbf{r_i})}{|\mathbf{r_{i+1}} - \mathbf{r_i}|}, \tag{27}$$

written here for the bond that joins particle i to particle $i+1$. In this equation, $d_{i,i+1} = |\mathbf{r_{i+1}} - \mathbf{r_i}|$ is the separation of particle i from particle $i+1$. The probability distribution $P(\phi)$ for ϕ_i at the beginning of stretching a sample at $F = 20$ is shown in Fig. 13. Since the force on i and $i+1$ depend also on the position of particle $i-1$ and particle $i+2$, there is no one-to-one correspondence between ϕ_i and the bond length. We verified, however, that the largest contribution to ϕ_i comes from the direct $i-(i+1)$ interaction, which, in our model, is automatically directed along the bond. The asymmetry in the ϕ distribution, therefore, is due to the asymmetry of the Morse potential, and the large fluctuations of ϕ_i reflect primarily the spectrum of stretching vibrations along the chains. We also verified that large positive ϕ_i values correspond to highly compressed bonds that are poised to rebound. Conversely, the (slightly) narrower distribution at $\phi_i \leqslant 0$ corresponds to stretched bonds, whose breaking is opposed by the Morse potential acting between i and $i+1$. Moreover, the probability distribution for ϕ_i does not depend much on the load F and is nearly constant during the entire span of our simulations, with, possibly, only a slight shift towards more negative values just before breaking. These results confirms that the conditions of our simulations correspond to relatively weak loads, with bond breaking driven primarily by thermal activation and only moderately biased by the applied tension.

A better prognostic value might be attributed to the distribution of *external* forces acting on each bond that differ from the previous case by the exclusion of the direct interaction between i and $i+1$. As expected, the new parameter:

$$\nu_i = \phi_i - 2\nabla V_M(|\mathbf{r_{i+1}} - \mathbf{r_i}|) \tag{28}$$

has a narrower and nearly symmetric distribution, as shown in Fig. 13 [V_M is the Morse potential of Eq. (2)]. Because

of its definition, the ν_i parameter can be interpreted as the external force on the bond that has to be balanced by the direct interaction to prevent breaking. Since the direct force between beads is limited to $|f_{\max}| = \max\{f^+ - f^-\} = a_0 D_0$, the integral of $P(\nu)$ from $f_{\max}$ to infinity gives the portion of the bond population that is likely to fail. For completeness, we monitor both I_ν^+ and I_ν^-, defined as:

$$I_\nu^+ = \int_{f_{\max}}^{\infty} P(\nu)d\nu \quad I_\nu^- = \int_{-\infty}^{-f_{\max}} P(\nu)d\nu. \tag{29}$$

These quantities now depend on F [see Fig. 13(b)] and change systematically and nearly monotonically with time, displaying a marked anomaly in the final avalanche stage of breaking. Admittedly, these features are not overwhelming, but, since they measure the fraction of bonds subject to comparatively high stress, the I_ν^+ and I_ν^- parameters might be monitored by spectroscopic means, providing a diagnostic tool in those cases in which simpler parameters (such as the global or local strain) cannot be measured directly or sufficiently accurately.

In experiments, the proximity and then the progression of failing in fibrous bundles is monitored by detecting the crackling noise emitted by the sample [46]. In our model, we do not have an unambiguous definition of *acoustic* emission. However, we tentatively monitor the square amplitude (power spectrum) of the time-dependent oscillations in the length $L_z(t)$ of individual bundles at a frequency ν that approaches the time scale ($\delta t = 2\pi/\nu = 450$ time units) of spontaneous and weakly damped oscillations of our samples. At the very least, these oscillations of the bundle length represent the longest-wavelength longitudinal vibrational (quasi-)eigenmode in our simulated system that is the most likely to couple to acoustic waves in the environment. More precisely, we compute and plot the time-dependent function:

$$|A|^2(t) = \left| \int_{t-\delta t}^{t+\delta t} g(t')e^{-i\nu t'}dt' \right|^2, \tag{30}$$

where $g(t')$ is defined on the time window $t - \delta \leqslant t' \leqslant t + \delta$ as:

$$g(t') = L_z(t') - \Big\{ L_z(t-\delta) + \frac{(t'-t+\delta)}{2\delta}[L_z(t+\delta) - L_z(t-\delta)] \Big\}. \tag{31}$$

In other terms, $g(t')$ reproduces the variations of $L_z(t')$, minus a linear term introduced to enforce the boundary conditions: $g(t-\delta) = g(t+\delta) = 0$. The results (not shown) display a large, nearly divergent increase of $|A|^2(t)$ for $t \longrightarrow \tau_i$ and show also a sequence of broad peaks distributed over the entire lifetime of the sample, somewhat increasing in frequency and intensity with increasing time. By direct comparison with the plot of $|z_b - z_a|_j(t)$ for individual sample j, it is easy to find correlations between the intensity peaks and increased fluctuations in the bundle length. This correspondence is certainly not unexpected, but at least it points to a possible mechanism of sound generation and suggests a relation between crackling noise and low-amplitude oscillations in the bundle length that otherwise might not be easy to detect.

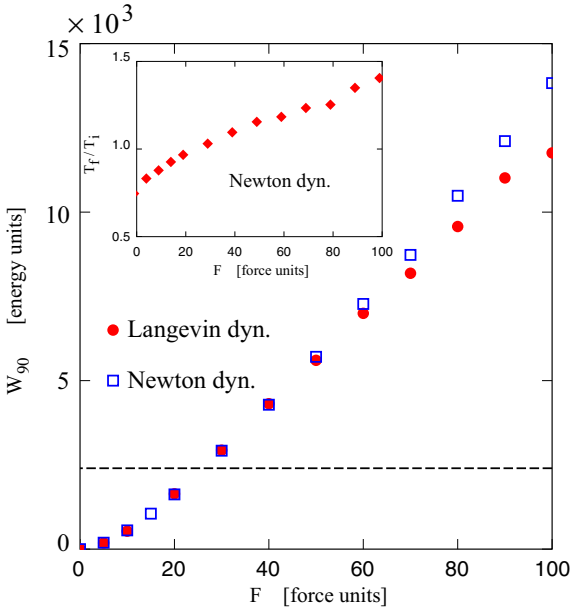

FIG. 14. (Color online) Work W_{90} performed by the external load to break 90% of the bundle chains (see text). The dashed line at $W_{90} = 2400$ corresponds to the energy $D_0 \times N_c$ required to break N_c bonds, thus representing the minimum energy needed to break a bundle. Inset: Ratio of temperatures at the end (T_f) and at the beginning (T_i) of the simulations based on Newton's equations of motion.

The work W performed by the external load on the bundle is computed by its most basic definition in terms of force and displacements. To limit the size of the fluctuations in breaking the last few chains, we focus on the work W_{90} required to break 90% of the bundle chains. The results are displayed in Fig. 14. By definition, W_{90} vanishes at $F = 0$, and at moderate loading it increases with F like $W_{90} \propto F^\gamma$; $\gamma > 1$. At higher F, the work W_{90} displays a clear linear ($W_{90} \sim F$) behavior that eventually has to level off since a finite amount of energy is sufficient to break all bonds.

We verified that, at low F, the work carried out by the external force is insufficient to break at least one bond per chain, which represents the minimum energy cost of breaking the bundle, and it is well below the energy stored in the broken bonds ($[n_{bb}(\tau) \gg n_{bc}(\tau) = N_c]$ at the end of our simulations. The situation is reversed at high values of F, in such a case the work done by F being 4 times the energy irreversibly spent to break bonds. Since the temperature of all samples is virtually unchanged throughout all simulations, the energy balance has to rely on the Langevin thermostat, which at low F supplies energy to the bundle, while at high F it adsorbs a portion of its (free) energy. The kinetic energy in the broken pieces at $t = \tau$ accounts for a relatively small fraction of the work done on the system by the external force. Admittedly, the Langevin thermostat affects significantly the balance of external work and dissipation into the different degrees of freedom. For this reason, this aspect will be analyzed in more detail by simulations without the Langevin thermostat.

The influence of the chain length, or, more precisely, of the number N_b of beads (and bonds) per chain on the breaking

process can be predicted on the basis of the simple model described at the beginning of this section. Assuming that bonds break independently at a constant rate, the lifetime of chains decreases like $1/N_b$, giving rise to the $\tau \sim N_b^{-\beta}$, $\beta \sim 1$ in the $f_1 \longrightarrow 0$ limit observed in Refs. [26–28]. At high load, however, the role of thermal degradation of bonds is reduced compared to the effect of the tensile load, and the time to break a chain depends less and less on its length, leading to the $\tau \sim N_b^{\beta}$, $\beta \longrightarrow 0$ of Refs. [26–28], again in the high-load regime. The results of our simulations, carried out at $T = 0.33$ for $80 \leqslant N_b \leqslant 200$, conform to these predictions, but even at $F = 100$ the β exponent estimated from our data is still closer to one than to zero, confirming that our virtual experiments always remained in a regime of moderate perturbation of the system dynamics.

The results of these last simulations provide a simple framework to predict or understand the effect of polydispersivity on the lifetime of bundles made of chains of unequal length. Let us assume that the length $N_b(i)$ of individual chains in the bundle is distributed according to $P[N_b]$. At the condition of our simulations, in which bonds break primarily by thermal activation, the longest chains break first, narrowing the length distribution towards the low-N_b range covered by $P[N_b]$. Test computations carried out for $100\sqrt{\langle \Delta_2 N_b \rangle}/\langle N_b \rangle = 20\%$ (with $\langle N_b \rangle = 100$) and following the same protocol of the other (monodisperse) simulations confirm again our expectations. The result will be different at high load, since in that case short chain are expected to fail first.

C. Results from simulations based on Newton's equations of motion

We now turn to the results of simulations in which particles are decoupled from the Langevin thermostat ($\eta = 0$ and no random forces). Simulations have been started from the same samples equilibrated at $T = 0.33$ already used for the Langevin simulations.

Under nonequilibrium conditions, there is no rigorous analog of the equivalence of different ensembles as in the equilibrium case. Nevertheless, the picture provided by this second set of computations, which we will call Newtonian to distinguish them from the Langevin ones, is recognizable as largely corresponding to the Langevin case, while fluctuations in the measured properties tend to differ in a more substantial way for the two choices of the system dynamics. In particular, the three basic facts described in the first part of this section are still valid: (i) the important role of the thermal breaking of bonds; (ii) the decrease of chain breaking rate due to the decreasing probability that a bond breaking takes place on a chain still intact; and (iii) the compensation of this effect by the dependence of the bond breaking rate on the tension per chain that increases while the number of broken chains decreases. However, two new factors come into play, i.e., the work carried out by the external force, that cannot be transferred to the bath, and the fact that the irreversible deformation of the system represented by broken bonds is a sink of potential energy. The two effects are competing with each other, and the prevailing one can be monitored by the change of temperature throughout the bundle breaking, which is shown in the inset of Fig. 14.

Our results show that, at low F, the thermal evaporation of bonds is the dominant feature, as shown by the decrease of temperature during the stretching simulation. At high F, the work performed by the external force prevails, increasing the sample temperature. These two opposite behaviours match at $F = 50$, which thus represents the natural separation of the low- and high-load regimes. These observations are reflected into the relative lifetimes of bundles in Langevin and in Newtonian simulations. At low F, in particular, the cooling during Newtonian stretching extends the sample lifetime (see Fig. 10), while at high F, heating makes Newtonian lifetimes shorter than their counterparts in Langevin simulations.

The number N_c of chains in the bundle represents the minimum number of broken bonds required to split the sample into two independent moieties. As expected, the number of broken bonds $n_{bb}(\tau)$ at the end of each simulation exceeds this minimum value, and the excess number $\Delta n_{bb} = n_{bb}(\tau) - N_c$ depends on F and on the dynamics adopted to carry out the time evolution. In the Langevin simulations, Δn_{bb} can be as large as $2N_c$ for $F \leqslant 15$, decreasing to $0.25N_c$ at $F = 100$. At moderate load, the Δn_{bb} from the Newtonian simulations is similar to the Langevin value $\Delta n_{bb} \sim 2N_c$, while it is roughly twice as large than its Langevin counterpart at high load, reaching $0.6N_c$ for $F = 100$.

During our Newtonian simulations, we recomputed the work W_{90} performed by the external load to break 90% of the bundle chains. The results have been added in Fig. 14 to compare with the data from the Langevin simulations. At low load, the two sets of results are the same to within the error bar, while at high load the W_{90} measured in the Newtonian simulations exceeds the corresponding W_{90} from Langevin simulations. This result is somewhat counterintuitive, since at high F the Langevin thermostat removes heat from the system. We do not have an unambiguous explanation for this observation, but the difference in Δn_{bb} at high F, computed by use of Newtonian or by Langevin dynamics, easily accounts for this difference.

The last remark concerns the difference in fluctuations of the bundle lifetimes as estimated by Newtonian or Langevin dynamics, illustrated in Fig. 12. The dependence of the statistical uncertainty $\Delta\tau/\tau$ on the applied load F is opposite in the two cases, with the Langevin $\Delta\tau/\tau$ increasing quadratically with increasing F, while the Newtonian data display a similarly parabolic decrease with increasing F. Note that the Newtonian values for $F = 0$ and $F = 5$ ($\Delta\tau/\tau \sim 0.2$) are omitted from Fig. 12, because they exceed the scale of our plot, possibly pointing to a weak singularity in the $F \longrightarrow 0$ limit.

D. The role of broken bonds recombination

The assumption of irreversible breaking of chains is indeed satisfied in most experiments on polymeric systems, since covalent dangling bonds rapidly decrease their energy by combining with radical contaminants that are present even in the cleanest system. This is even more true for fibers in a wet environment, in which mobile OH_3^+ or OH^- species are present. In polymers, therefore, the reversible breaking and formation of bonds is quite exceptional, corresponding in fact to the special case of the so-called living polymers [47]. Although fairly restricted, this class of polymers is

conceptually very important and for this reason we briefly discuss here the consequences of reversible bond formation and breaking. Moreover, reversible bonding might be more important in other classes of soft materials such as emulsions and colloidal gels, in which each particle feels a multitude of weaker, isotropic interactions. The reversibility of their bonding is highlighted by their ability to undergo stages of extended structural healing through the so-called shear-rejuvenation process [48].

To simplify the computation and retain a favorable scaling of computer time with system size, we consider the special case in which each dangling bond can reconnect only with its original partner. From the chemical point of view, this is an arbitrary assumption, since dangling bonds are all equivalent and cannot be distinguished from each other. In practice, however, we are interested in systems in which the density of dangling bonds is low, and the only relevant possibility is that a broken bond quickly reforms, joining the original particles, before the two partners lose track of each other. At the very least, our simulations with restricted bond recombination allow us to highlight the qualitative differences with the no-recombination case and provide a first preliminary exploration of a rich new model.

At this stage of the computation, the lateral size of the sample is relevant, since it influences the probability of the two loose ends to recombine. Therefore, we introduce periodic boundary conditions along the in-plane x and y directions, setting the periodicity at $L_x = L_y = 20$, thus giving a 2D density of one chain per unit of area.

No major change in the system behavior is observed at high values of the applied force, since the breaking of chains causes a sizable increase of the bundle elongation, and the fast separation of the two loose ends, thus preventing recombination. With decreasing F, however, it is increasingly likely that the two chain terminations will remain close to each other long enough to have a significant chance of recombining. The change of behavior is relatively sharp and marked by the anomalous increase of fluctuations in the breaking time. Below a critical applied tension F_c, the sample does not appear to break within the time span accessible to simulation (see Fig. 15).

In our simulations, carried out with the same basic model of the previous sections, the critical load is found at $F^* \sim 48 \pm 3$. At this load, the time evolution of different samples can be very diverse, with cases in which the bundle starts immediately to break and cases in which the actual beginning of the breaking process is preceded by a lag time, as can be seen in the inset of Fig. 15.

On a much longer time scale, all samples will eventually break, since in that way they can tap the unlimited supply of entropy available from the open space. In proximity of the critical F^*, the system evolution can be seen as the uncertain competition of bond breaking, increasing elongation and decreasing recombination rates, and bond recombination that temporarily decreases elongation and reinforces itself. Even below F^*, a positive fluctuation in the bundle elongation can decisively decrease the recombination rate, tipping the balance in favor of bond breaking, leading to the bundle failing. A similar picture of bundle rupture under cyclic loading (fatigue) is discussed in Ref. [23].

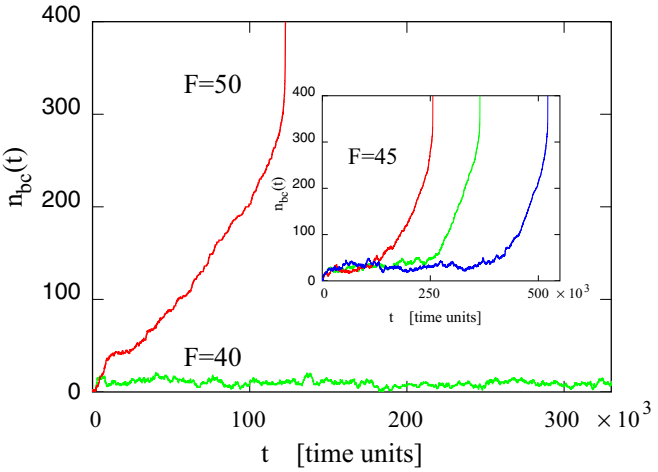

FIG. 15. (Color online) Simulations with bond recombination mechanism (see text): The number of broken chains as a function of time in two samples under tensile load above [(a) $F = 50$] and below [(b) $F = 40$] the critical load $F^* = 48$. Inset: Time dependence of the number of broken bonds in three distinct samples under the same (slightly subcritical) load $F = 45$.

Bond recombination, therefore, not only introduces a critical F^* tension, but also changes the nature of the bundle failing process that below F^* goes through a latency time, in preparation of the fluctuation that drives the bundle to its demise. This represents a kinetic nucleation process that deserves further extensive analysis by simulation, theory, and experiments.

E. Simulations at constant strain rate

The resistance of polymeric fiber bundles is sometimes investigated by experiments that, instead of applying a constant load, strain the sample at a constant rate up to its breaking point [49]. The basic result of these measurements is represented by the stress-strain relation for the material under study that depends on the temporal rate of strain applied to the sample.

To extend the validation envelop of our idealized model, we simulated samples under these same constant strain rate conditions, and we verified that the simulation results reflect basic features seen in the experimental data [31]. We used again the same bundles already described in Sec. III, each consisting of 400 chains 100 beads long. Molecular dynamics has been carried out in the Langevin framework, at a temperature $T = 0.33$, and no bond recombination was allowed. At this stage, the two terminations of each bundle move in opposite directions at constant velocity, according to:

$$z_a(t) = z_a(t_0) - R(t - t_0), \tag{32}$$

$$z_b(t) = z_b(t_0) + R(t - t_0). \tag{33}$$

The constant rate at which strain increases, therefore, is $2R$. Clamps do not react to changes in the bundle conformation and bonding, and therefore the mechanism for chain-chain interaction discussed in the previous sections is no longer present. Simulation of whole bundles (instead of individual chains) are used only to account for the interplay between the

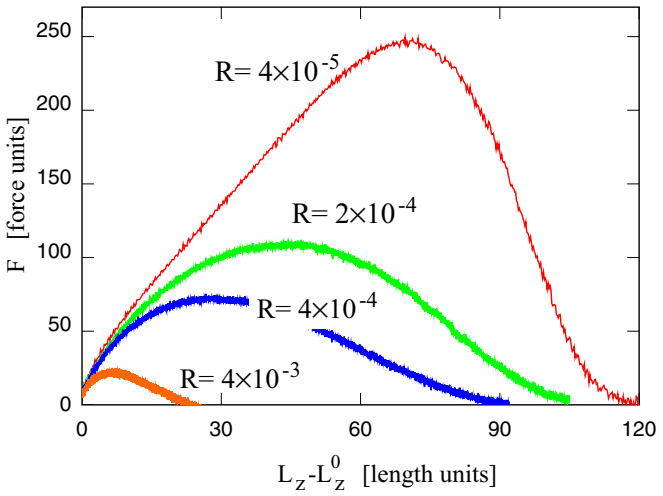

FIG. 16. (Color online) Stress-strain relation in samples simulated by Langevin dynamics at four values of constant strain rate (R) testing.

constant strain rate and the internal dynamics of a statistical assembly of independent chains.

The stress-strain characteristics of our model, averaged over 20 independent samples, are shown in Fig. 16 for strain rates $R = 10^{-6}$, $R = 5 \times 10^{-6}$, $R = 10^{-5}$, and $R = 10^{-4}$. Comparison with the results of recent experiments [31] shows a good qualitative correspondence of simulation and experimental results, with (i) an initial stage of a linear, Hooke's-like increase of stress with increasing strain; (ii) a broad region of viscoelastic deformation in which the stress grows only moderately despite the large increase of the bundle length; and (iii) a failing stage, in which increasing strain is opposed by a rapidly decreasing stress, caused by the low and rapidly decreasing number of chains that still survive.

The most remarkable feature of our results arguably is the strong influence of the strain rate on the maximum stress on the sample and also on the elongation (strain) at breaking. Such a strong dependence has two origins. Partly, it is due to the high rate of thermal breaking of bonds that degrades the resistance of our samples over time (aging). Moreover, low strain rates allow chains to unroll their Gaussian coiling without going through high-strain configurations. Including bead-bead interactions would enhance the role of this second effect.

These preliminary results confirm the qualitative validity of our idealized model also in this type of constant strain rate applications and highlight the interest of this type of investigation.

IV. SUMMARY AND CONCLUSIONS

Creep in polymeric fibers has been investigated by molecular dynamics simulations, using a particle-based realization of the fiber-bundle model to carry out the virtual testing of finite-size samples under subcritical tensile load.

In many respects, the model that we employ is a hybrid, introducing a coarse-grained representation of the polymer structure, and thus accounting for inertia, temperature, and entropy, but neglecting general particle-particle interactions besides the nearest-neighbor ones along the chain backbone. Its definition and usage has been tuned to provide a seamless junction between the statistical mechanics and material science picture of this technologically important phenomenon.

In this spirit, our computations have achieved a twofold goal. On the one hand, we verified that such a model retains the valuable fiber bundle model ability to faithfully reproduce and predict basic properties, trends, and features seen in the results of experiments probing creep in macroscopic samples. On the other hand, the thorough investigation of a still-idealized system allows us to set the stage for more detailed models, to test protocols for the sample preparation and usage, and to develop approaches to analyze the simulation results.

Simulations have been carried out for samples consisting of $N_c = 400$ chains, each consisting of $N_b = 100$ beads, clamped to two rigid planes mobile along the z direction perpendicular to their parallel faces. Because of the absence of general particle-particle interactions, chains interact only through their common termination on the planar clamps. We verified, however, that this peculiar contact is sufficient to ensure their equilibration within a time much shorter that the simulation times scale. The multiplicity of chains in our sample represents a major extension of previous studies investigating the breaking of single chains [26–28], bringing us one step closer to realistic models of creep in polymers.

Most of our simulations concerned samples under constant tensile load, but we also explored the other major condition of creep mechanical testing taking place at constant strain rate. Similarly, the majority of simulations excluded the recombination of bonds after their breaking, a condition reflecting the behavior of most polymeric systems. However, we also carried out a preliminary series of simulations to explore the effect of reversible breaking and formation that is certainly important in other soft matter systems such as emulsions and colloidal gels. The parameters of the model potential (bond length $r_e = 1.5$, potential well depth $D_0 = 6$, and elastic parameter $a_0 = 2$ in scaled units) as well as the simulation conditions (temperature, load) have been selected to cause the breaking of $\sim N_c$ bonds during runs of acceptable cost, allowing us to carry out the multiple simulations needed to compute average properties.

The immediate outcome of our study can be summarized as follows. First, the results of constant load and constant temperature simulations reproduce characteristic features of the primary, secondary, and tertiary stages of creep as observed in experiments on macroscopic samples [38–40]. In particular, the progressive lengthening of the bundle displays a first stage of fast and nearly reversible evolution, followed by a long stage of nonlinear deformation, in which the strain rate slows down significantly, attaining a minimum value well below the initial rate but eventually triggering the final avalanche that breaks the sample. Over the entire sample lifetime, the strain rate can be reproduced by a simple and general analytical expression, already extensively used in the literature to model creep [25]. The quantitative value of the parameters providing the best fit, however, differ from those found in experiments on comparable materials.

A similar succession of three stages can be identified in the time evolution of the number of broken chains. The first two stages, in particular, can be described in terms of a simple

model, based on the observation that the rate of thermal bond breaking is nearly constant. In this picture, the avalanche represent a singular behavior, responsible for most of the fluctuations in the simulation results.

A logarithmic plot of the bundles lifetime τ versus load F displays a marked curvature at low F, ruling out a simple power-law dependence of τ on F. At high load, however, the $\log(\tau)$-versus-$\log(F)$ plot approaches a straight line of slope $\alpha = -4$, reminiscent of a similar power-law relation observed in creep experiments on protein gels [25].

Without bond recombination mechanism, and in the absence of general particle-particle interactions, the lateral size of the sample and the application of periodic boundary conditions are irrelevant, although the number N_c of chains still affects the degree of fluctuations and cooperativity in the motion of the clamps, reflected in the short-time dynamics of the bundle length. Our results, therefore, could be interpreted in terms of finite-size samples and could provide a first description of mechanical properties of nanofibers, especially in a biophysics context.

The inclusion of bond recombination into the model qualitative changes the picture and introduces a critical load F^* that corresponds to the branching of the system evolution into two different patterns. Above F^* the system evolution is nearly deterministic, with a downhill progression towards the broken state and fluctuations whose amplitude grows when approaching F^*. Far below F^*, the sample does not break during the time span of practical simulations, although simple considerations suggest that the broken state is always the most stable configuration, while the intact bundle is metastable. Just below F^*, a lag time of seemingly unpredictable duration precedes the beginning of the actual breaking process, apparently needed to prepare for the critical density fluctuation that drives the system towards its stable state.

As a final step, we investigated the behavior of our samples stretched at constant strain rate. Also in this case, the simulation data reflect features seen in experimental results. The strain-stress relation, in particular, display again three distinct stages, in this case corresponding to (i) elastic deformation at low strain, (ii) a broad region of saturating stress, leading to (iii) a failure stage in which the few surviving chains oppose a rapidly decreasing resistance to the separation of two half bundles. The most remarkable feature seen in the simulation results is the nonlinear increase of the maximum stress and bundle length at the breaking point with increasing strain rate. The absence of general bead-bead interactions might be a factor that amplifies the nonlinearity in the system response.

The obvious next step in our long-term plan to characterize mechanical properties by computational means is the inclusion in our model of bead-bead interactions. These, in turn, will introduce excluded volume effects, entanglement, as well as phase changes and the coexistence of crystalline and amorphous fractions in our polymeric samples. A further step towards realism might involve the inclusion of an explicit solvent. Each of these additions will increase significantly the cost of the computations but will also open the way to a more quantitative comparison with experiments, extending our investigations towards a variety of other phenomena, such as plasticity and crazing, that are now beyond the reach of our simulations.

[1] Leonardo da Vinci, *Codex Atlanticus* (U. Hoepli, Milano, 1894).

[2] A. A. Griffith, Phil Trans. R. Soc. (Lond.) A **221**, 163 (1920).

[3] V. S. Kuksenko and V. P. Tamuzs, *Fracture Micromechanics of Polymer Materials* (Springer-Verlag, Berlin, 1981).

[4] B. R. Lawn, *Fracture of Brittle Solids* (Cambridge University Press, Cambridge, 1993).

[5] W. Grellmann and S. Seidler, *Deformation and Fracture Behavior of Polymers* (Springer-Verlag, Berlin, 2001).

[6] T. L. Anderson, *Fracture Mechanics: Fundamentals and Applications, Third Edition* (CRC Press, Boca Raton, FL, 2004).

[7] H. J. Herrmann and S. Roux, *Statistical Models for the Fracture of Disordered Media* (Elsevier, Amsterdam, 1990).

[8] B. K. Chakrabarti and L. G. Benguigui, *Statistical Mechanics of Fracture and and Breakdown in Disordered Systems* (Oxford University Press, Oxford, 1997).

[9] M. J. Alava, P. K. V. V. Nukala, and S. Zapperi, Adv. Phys. **55**, 349 (2006).

[10] D. Bonamy and E. Bouchaud, Phys. Rep. **498**, 1 (2011).

[11] T. T. Chiao, C. C. Chiao, and R. J. Sherry, in *Fracture Mechanics and Technology*, edited by G. C. Sih and C. L. Chow (Sijthoff and Noordhoff, Amsterdam, 1977), Vol. 1, p. 257.

[12] J. Schmittbuhl and K. J. Måløy, Phys. Rev. Lett. **78**, 3888 (1997).

[13] D. S. Farquhar, F. M. Mutselle, S. L. Phoenix, and R. L. Smith, J. Mater. Sci. **24**, 2151 (1989).

[14] H. Otani, S. L. Phoenix, and P. Petrina, J. Mater. Sci. **26**, 1955 (1991).

[15] M. J. Buehler, *Atomistic Modeling of Materials Failure* (Springer-Verlag, Berlin, 2008).

[16] J. Yao, C. W. M. Bastiaansen, and T. Peijs, Fibers **2**, 158 (2014); **28**, 1065 (1957).

[17] F. T. Peirce, J. Textile Inst. **17**, T355 (1926).

[18] H. E. Daniels, Proc. R. Soc. London A **183**, 405 (1945).

[19] S. Pradhan, A. Hansen, and B. K. Chakrabarti, Rev. Mod. Phys. **82**, 499 (2010).

[20] A. Hansen, P. C. Hemmer, and S. Pradhan, *The Fiber Bundle Model* (Wiley, New York, 2015).

[21] L. Mishnaevski, *Computational Mesomechanics of Composites* (Wiley, New York, 2007).

[22] L. Mishnaevski and P. Brønsted, Comp. Mater. Sci. **44**, 1351 (2009).

[23] F. Kun, H. A. Carmona, J. S. Andrade Jr., and H. J. Herrmann, Phys. Rev. Lett. **100**, 094301 (2008).

[24] A. M. Saitta, P. D. Soper, E. Wasserman, and M. L. Klein, Nature **399**, 46 (1999); A. M. Saitta and M. L. Klein, J. Phys. Chem. B **104**, 2197 (2000).

[25] M. Leocmach, C. Perge, T. Divoux, and S. Manneville, Phys. Rev. Lett. **113**, 038303 (2014).

[26] J. Paturej, A. Milchev, V. G. Rostiashvili, and T. A. Vilgis, Europhys. Lett. **94**, 48003 (2011).

[27] J. Paturej, A. Milchev, V. G. Rostiashvili, and T. A. Vilgis, J. Chem. Phys. **134**, 224901 (2011).
[28] F. A. Oliveira and P. L. Taylor, J. Chem. Phys. **101**, 10118 (1994).
[29] P. G. de Gennes, *Scaling Concepts in Polymer Physics* (Cornell University Press, Ithaca, 1979); G. R. Strobl, *The Physics of Polymers* (Springer-Verlag, Heidelberg, 2007).
[30] N. Grønbech-Jensen and O. Farago, Mol. Phys. **111**, 983 (2013).
[31] D. L. Languerand, H. Zhang, N. S. Murthy, K. T. Ramesh, and F. Sansoz, Mater. Sci. Eng. A **500**, 216 (2009).
[32] N. W. Ashcroft and N. D. Mermin, *Solid State Physics* (Holt-Saunders, Fort Worth, TX, 1976).
[33] F. Kun, R. C. Hidalgo, H. J. Herrmann, and K. F. Pál, Phys. Rev. E **67**, 061802 (2003).
[34] The Arrhenius fit of the rate of bond breaking at $T = 0.30$, $T = 0.33$, and $T = 0.36$ shows that the free-energy barrier to break single bonds at tension $F = 40$ is $\Delta_a \sim 5$ (energy units), i.e., not much different from the cohesive energy per bond at $T = 0.33$. This close correspondence of activation and cohesive energy points to a relatively small role of entropy in the breaking process.
[35] B. D. Coleman, J. Appl. Phys. **27**, 862 (1956).
[36] At $F = 0$ the growth of bundle elongation $|z_b - z_a|$ with time is caused by the pressure on the soft repulsive walls [Eq. (8)] from the broken chains and loose chain segment trapped in between.
[37] L. C. E. Struik, Rheol. Acta **6**, 119 (1967).
[38] N. G. McCrum, C. P. Buckley, and C. B. Bucknall, *Principles of Polymer Engineering* (Oxford Science, Oxford, 2003).
[39] M. A. Meyers and K. K. Chawla, *Mechanical Behavior of Materials* (Cambridge University Press, Cambridge, 1999).
[40] E. N. da Costa Andrade, Proc. R. Soc. Lond. A **84**, 1 (1910).
[41] A. Jaishankar and G. H. McKinley, Proc. R. Soc. A **469**, 20120284 (2013).
[42] F. Gobeaux, E. Belamie, G. Mosser, P. Davidson, and S. Asnacios, Soft Matter **6**, 3769 (2010).
[43] F. C. Monkman and N. J. Grant, Proc. Am. Soc. Test. Mater. **56**, 593 (1956).
[44] A. Guarino, S. Ciliberto, A. Garcimartín, M. Zei, and R. Scorretti, Eur. Phys. J. B **26**, 141 (2002).
[45] O. H. Basquin, Proc. Am. Soc. Test. Mater. **10**, 625 (1910).
[46] R. El Guerjouma, J.-C. Baboux, D. Ducret, N. Godin, P. Guy, S. Huguet, Y. Jayet, and T. Monnier, Adv. Eng. Mater. **3**, 601 (2001).
[47] S. C. Greer, Annu. Rev. Phys. Chem. **53**, 173 (2002).
[48] T. Divoux, V. Grenard, and S. Manneville, Soft Matter **8**, 4151 (2012).
[49] B. A. Gama, S. L. Lopatnikov, and J. J. W. Gillespie, Appl. Mech. Rev. **57**, 223 (2004).